The Astrophysical Journal Letters, 977:L6 (7pp), 2024 December 10 https://doi.org/10.3847/2041-8213/ad91a3

The Impact of Shear on Disk Galaxy Star Formation Rates

Xena Fortune-Bashee[1], Jiayi Sun (孙嘉懿)[2,4], and Jonathan C. Tan[1,3]
[1] Department of Astronomy, University of Virginia, 530 McCormick Road, Charlottesville, VA 22904, USA
[2] Department of Astrophysical Sciences, Princeton University, 4 Ivy Lane, Princeton, NJ 08544, USA
[3] Department of Space, Earth & Environment, Chalmers University of Technology, Gothenburg, Sweden
Received 2024 September 11; revised 2024 November 07; accepted 2024 November 08; published 2024 December 2

Abstract

Determining the physical processes that control galactic-scale star formation rates is essential for an improved understanding of galaxy evolution. The role of orbital shear is currently unclear, with some models expecting reduced star formation rates and efficiencies with increasing shear, e.g., if shear stabilizes gas against gravitational collapse, while others predicting enhanced rates, e.g., if shear-driven collisions between giant molecular clouds trigger star formation. Expanding on the analysis of 16 galaxies by C. Suwannajak et al., we assess the shear dependence of star formation efficiency (SFE) per orbital time ($\epsilon_{\rm orb}$) in 49 galaxies selected from the PHANGS-ALMA survey. In particular, we test a prediction of the shear-driven giant molecular cloud (GMC) collision model that $\epsilon_{\rm orb} \propto (1–0.7\beta)$, where $\beta \equiv d\ \ln v_{\rm circ}/d\ \ln r$, i.e., SFE per orbital time declines with decreasing shear. We fit the function $\epsilon_{\rm orb} = \epsilon_{\rm orb,0}(1 - \alpha_{\rm CC}\beta)$ finding $\alpha_{\rm CC} \simeq 0.76 \pm 0.16$; an alternative fit with $\epsilon_{\rm orb}$ normalized by the median value in each galaxy yields $\alpha^*_{\rm CC} = 0.80 \pm 0.15$. These results are in good agreement with the prediction of the shear-driven GMC collision theory. We also examine the impact of a galactic bar on $\epsilon_{\rm orb}$ finding a modest decrease in SFE in the presence of a bar, which can be attributed to lower rates of shear in these regions. We discuss the implications of our results for the GMC life cycle and environmental dependence of star formation activity.

Unified Astronomy Thesaurus concepts: Star formation (1569); Galaxy dynamics (591); Disk galaxies (391); Interstellar medium (847)

1. Introduction

The star formation rate (SFR) of galactic disks is of fundamental importance to the evolution of these systems and to galaxy evolution in general. Correlations between SFR, gas content, and galactic dynamical properties have been found on both global and local, i.e., $\lesssim$kiloparsec, scales (e.g., R. C. Kennicutt & N. J. Evans 2012; E. Schinnerer & A. K. Leroy 2024). These are typically expressed in the form of "star formation laws." For example, the Kennicutt–Schmidt (KS) law takes the form $\Sigma_{\rm SFR} \propto \Sigma_{\rm gas}^{\alpha_g}$, where $\Sigma_{\rm SFR}$ is the disk plane surface density of SFR and $\Sigma_{\rm gas}$ is the total (atomic + molecular) gas mass surface density. Superlinear values of $\alpha_g \simeq 1.5$ have been found (e.g., R. C. J. Kennicutt 1998; R. C. Kennicutt & N. J. Evans 2012).

The "dynamical KS" law (or "Silk–Elmegreen" law; B. G. Elmegreen 1997; J. Silk 1997) takes the form

$$\Sigma_{\rm SFR} = B_\Omega \Sigma_{\rm gas} \Omega, \tag{1}$$

where Ω is the galactic orbital angular frequency and B_Ω is a dimensionless normalization constant. R. C. J. Kennicutt (1998) found this was an equally good description of a sample of disk-averaged measurements of galactic disks and circumnuclear starbursts (see also, e.g., A. K. Leroy et al. 2008; J. C. Tan 2010; J. Sun et al. 2023). Such a dynamical KS law has been proposed to arise naturally if large-scale galactic dynamical processes, such as spiral arm passage (e.g., R. F. G. Wyse & J. Silk 1989) or growth of large-scale instabilities (e.g., B. G. Elmegreen 1991), are the rate-limiting step for star formation.

However, considering that most star formation occurs in highly clustered $\sim$1–10 pc regions within giant molecular clouds (GMCs), J. C. Tan (2000) proposed shear-driven GMC–GMC collisions in a Toomre $Q \sim 1$, flat rotation curve disk could also explain the dynamical KS law. The key prediction of this theory is that $\Sigma_{\rm SFR}$ is related to the galactic orbital period and shear via[5]

$$\Sigma_{\rm SFR} = B_\Omega\ \Sigma_{\rm gas}\ \Omega(1\ -\ 0.7\beta), \tag{2}$$

where $\beta \equiv d\ \ln v_{\rm circ}/d\ \ln r$ is the logarithmic derivative of the rotation curve $v_{\rm circ}(r)$, i.e., taking the value $\beta = 1$ in the flat rotation curve case. Higher β values, closer to the solid body rotation case of $\beta = 1$, imply lower orbital shear strength, consistent with alternative formulations with Oort's constants (see, e.g., J. Binney & S. Tremaine 1987).

J. C. Tan (2010) carried out a test of the shear-driven GMC law, along with five other star formation laws, against a sample of 12 nearby, resolved disk galaxies, focusing on molecular-rich regions, i.e., with $\Sigma_{\rm H2} \gtrsim \Sigma_{\rm H\,I}$. The shear-driven law (Equation (2)) was found to be more favored than the simple dynamical KS law (Equation (1)), although two other SF laws, i.e., a "molecular KS" law with $\Sigma_{\rm SFR}$ proportional to molecular gas mass surface density and the "turbulence-regulated" law of M. R. Krumholz et al. (2009), gave similarly good fits to the data. C. Suwannajak et al. (2014) followed up this study by

[4] NASA Hubble Fellow.

[5] Note that Equation (2) was derived via a first-order expansion in β (i.e., valid for $\beta \lesssim 0.5$).

examining 16 galaxies, demonstrating with high significance that higher shear rates correlate with higher SFRs and star formation efficiencies (SFEs) per local orbital time, $\epsilon_{\rm orb}$. A modestly higher (by a factor of 1.3) average value of $\epsilon_{\rm orb}$ was found in the subsample of barred galaxies compared to the nonbarred sample. However, this modest enhancement was not statistically significant given the small sample sizes.

Here we test the prediction of Equation (2) with higher-quality data for a sample of 49 galaxies. We present our methods in Section 2, our results in Section 3, and a summary and discussion in Section 4.

2. Method

We test Equation (2) using observations of $\Sigma_{\rm SFR}$, $\Sigma_{\rm gas}$, Ω, and β in 49 galaxies from the PHANGS-ALMA survey (A. K. Leroy et al. 2021). We extract these measurements from machine-readable tables (version 4.0; J. Sun et al. 2022), reported as azimuthal averages in 500 pc wide radial bins across each galaxy (see Section 3.1 therein). Here we briefly describe how these quantities were derived and refer readers to J. Sun et al. (2022) for more details. Values of $\Sigma_{\rm SFR}$ were derived by combining ground-based Hα narrowband and Wide-field Infrared Survey Explorer 22 μm imaging data, following the calibration by F. Belfiore et al. (2023). $\Sigma_{\rm mol}$ was derived from PHANGS-ALMA CO(2–1) observations (A. K. Leroy et al. 2021) using a metallicity-dependent CO-to-H_2 conversion factor (J. Sun et al. 2020b, 2020a). $\Sigma_{\rm atom}$ was derived from a compilation of the literature and new H I 21 cm observations, including THINGS (F. Walter et al. 2008), VIVA (A. Chung et al. 2009), VLA-HERACLES (A. K. Leroy et al. 2012), and PHANGS-VLA (PI: D. Utomo). All these surface density measurements are corrected for galaxy inclination. Lastly, $v_{\rm circ}$ and β were based on CO kinematics (P. Lang et al. 2020), or more specifically, smooth functional fits to the observed CO rotation curves (E. Rosolowsky 2024, private communication; see detailed descriptions in J. Sun et al. 2022).

We use these measurements to test Equation (2) by recasting it into the following form (also see J. C. Tan 2010; C. Suwannajak et al. 2014):

$$\epsilon_{\rm orb} \equiv \Sigma_{\rm SFR}\, t_{\rm orb}/\Sigma_{\rm gas} = 2\pi B_\Omega (1 - 0.7\beta), \quad (3)$$

where $t_{\rm orb} = 2\pi/\Omega$ is orbital period and $\epsilon_{\rm orb}$ is dimensionless SFE per orbit. We derive $\epsilon_{\rm orb}$ and β for each radial bin in each galaxy and assess if their relationship can be well described by Equation (3).

We note that the original formulation of the J. C. Tan (2000) model considers total gas mass surface density, $\Sigma_{\rm gas}$, as the relevant parameterization of the gas reservoir. Nonetheless, recent works find $\Sigma_{\rm SFR}$ correlates more strongly with $\Sigma_{\rm mol}$, suggesting a tighter link between star formation and molecular gas (e.g., F. Bigiel et al. 2008; A. K. Leroy et al. 2008; A. Schruba et al. 2011). Besides, the limited availability of H I 21 cm data for the PHANGS-ALMA galaxy sample (see J. Sun et al. 2022, for a compiled list) means we can only derive $\Sigma_{\rm gas} = \Sigma_{\rm mol} + \Sigma_{\rm atom}$ for a subsample of 32 galaxies, whereas we have $\Sigma_{\rm mol}$ measurements for 49. Given these considerations, we use two operational definitions for SFE per orbit:

$$\epsilon_{\rm orb} \equiv \Sigma_{\rm SFR}\, t_{\rm orb} \,/\, \Sigma_{\rm gas}, \quad (4)$$

$$\epsilon_{\rm orb,mol} \equiv \Sigma_{\rm SFR}\, t_{\rm orb} \,/\, \Sigma_{\rm mol}. \quad (5)$$

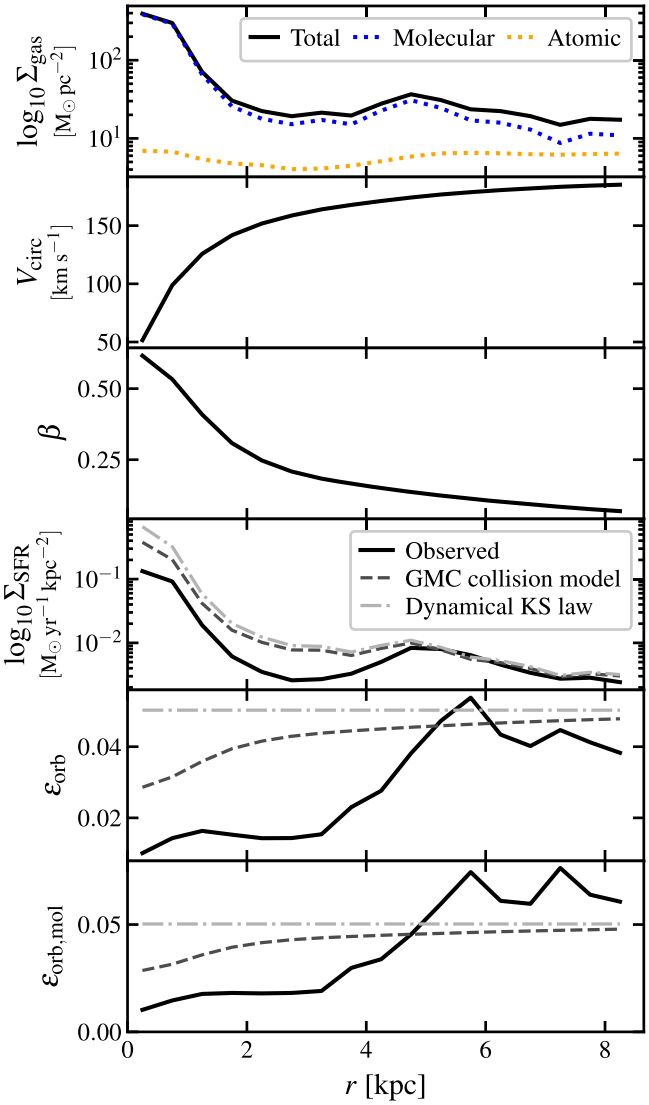

Figure 1. Example data set for NGC 4321. The top panel shows the radial profile of mass surface density of total (black solid), molecular (blue dotted), and atomic gas (orange dotted). The second and third panels show orbital velocity and its logarithmic derivative, β. The fourth panel shows the observed SFR surface density profile (solid) and theoretical predictions of the J. C. Tan (2000) shear-driven GMC collision model, $\Sigma_{\rm SFR} = B_\Omega \Sigma_{\rm gas}\Omega(1–0.7\beta)$ (dashed), and the dynamical KS model (B. G. Elmegreen 1997; J. Silk 1997) with a fixed SFE per orbit, i.e., $\Sigma_{\rm SFR} = B_\Omega \Sigma_{\rm gas}\Omega$ with $B_\Omega = 8 \times 10^{-3}$ (dotted). The fifth panel shows observed SFE per orbit with reference to the total gas as well as theoretically predicted values (the same models as in the fourth panel). The sixth panel is the same as the fifth, but now showing SFE per orbit with reference to the molecular gas.

We derive each of these for as many galaxies and radial bins as allowed by data availability and examine their relationships with β.

3. Results

3.1. Impact of Shear on Star Formation

Figure 1 shows example data for galaxy NGC 4321. In particular, the fourth panel shows the observed SFR surface density compared to the SFR surface density predicted by the shear-driven GMC collision model (Equation (2)) with $B_\Omega = 8.0 \times 10^{-3}$, which corresponds to a flat rotation curve ($\beta = 0$) limiting value of $\epsilon_{\rm orb} = 2\pi B_\Omega = 0.05$. The prediction of

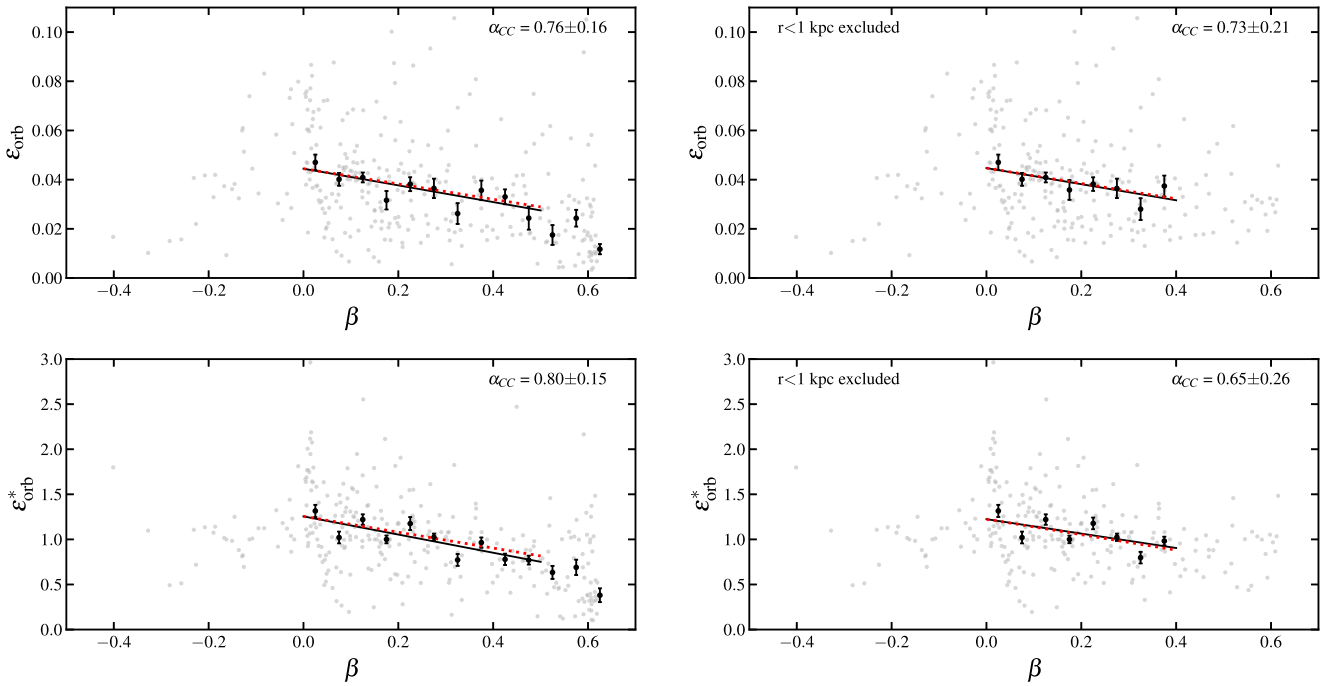

Figure 2. (a) Top left: total SFE per orbit, ϵ_{orb}, vs. rotation curve gradient, β, for 321 annuli located in 32 PHANGS-ALMA galaxies with observations probing molecular and atomic gas (gray points). Black points show the median values of ϵ_{orb} in bins of $\Delta\beta = 0.05$ that have at least 10 data points, with associated error bars showing the uncertainties in the median. The solid black line shows the best-fit function of the form $\epsilon_{orb} = \epsilon_{orb,0}(1 - \alpha_{CC}\beta)$ to the binned medians with $\beta \leqslant 0.5$, with α_{CC} reported in the upper right corner of each panel. The red dotted line shows the equivalent fit with a fixed $\alpha_{CC} = 0.7$, i.e., the prediction of the shear-driven GMC collision model. (b) Top right: as (a), but now excluding annuli within $r = 1$ kpc. (c) Bottom left: as (a), but with ϵ_{orb} normalized by the median value of each galaxy (i.e., "galaxy-normalized" ϵ^*_{orb}). (d) Bottom right: as (c), but now excluding annuli within $r = 1$ kpc. A trend of declining efficiency with increasing β is seen in all cases.

the simpler dynamical KS model (Equation (1)), with ϵ_{orb} independent of β, is shown by the dotted line. The fifth panel shows the observed SFE per orbit with reference to total gas, ϵ_{orb}, and the predictions from the above two theoretical models. The sixth panel shows the equivalent results for SFE per orbit with reference to molecular gas, $\epsilon_{orb,mol}$. The data shown in Figure 1 indicate that there is a reduced SFE per orbit in regions of lower shear, i.e., higher β.

In Figure 2(a) we plot ϵ_{orb} versus β across 321 independent annuli in 32 PHANGS-ALMA galaxies. We evaluate median values of ϵ_{orb} in bins of uniform width $\Delta\beta = 0.05$, excluding bins with <10 data points. These binned medians are shown with black points, along with their uncertainties.

Next, for all binned medians with $\beta \leqslant 0.5$,[6] we fit a function:

$$\epsilon_{orb} = \epsilon_{orb,0}(1 - \alpha_{CC}\beta), \quad (6)$$

where $\epsilon_{orb,0}$ is the value of ϵ_{orb} in the flat rotation curve limit of $\beta = 0$. The results are $\epsilon_{orb,0} = 0.045 \pm 0.002$ and $\alpha_{CC} = 0.76 \pm 0.16$, shown by the solid black line in Figure 2(a). These fit parameters are insensitive to choices of bin width in β and consistent with alternative, nonparametric methods for reconstructing the median trends. An equivalent fit in which α_{CC} is fixed at 0.7, i.e., the predicted value of the shear-driven GMC collision model, is shown by the red dotted line. We see that the observed dependence of ϵ_{orb} versus β agrees well with the theoretical prediction.

[6] This choice, following C. Suwannajak et al. (2014), avoids the regime where β is no longer significantly smaller than unity, where Equation (2) is no longer a good approximation (see Section 1).

Next, we repeat this analysis, but excluding the innermost 1 kpc of each galaxy (Figure 2(b)). These regions have the most uncertain rotation curve measurements (e.g., due to significant noncircular motions) and thus values of β. They may also have the largest systematic uncertainties in gas masses and SFRs. These excluded regions tend to have high values of β and so the remaining data are now insufficient to measure median values for $\beta > 0.4$. Nevertheless, the impact on the derived parameters appears minimal, with $\epsilon_{orb,0} = 0.045 \pm 0.002$ and $\alpha_{CC} = 0.73 \pm 0.21$.

Next, in Figure 2(c), we consider "galaxy-normalized efficiencies," i.e., $\epsilon^*_{orb} \equiv \epsilon_{orb}/\overline{\epsilon_{orb}}$, where $\overline{\epsilon_{orb}}$ is the galaxy-wide median value of ϵ_{orb}, i.e., among all annuli of a given galaxy. This method, following C. Suwannajak et al. (2014), gives an extra degree of freedom in the normalization of each galaxy and so yields a more accurate measure of the relative dependence of ϵ_{orb} with β for the global sample. We fit the function:

$$\epsilon^*_{orb} = \epsilon^*_{orb,0}(1 - \alpha^*_{CC}\beta), \quad (7)$$

and derive $\alpha^*_{CC} = 0.80 \pm 0.15$. Figure 2(d) presents the equivalent results when the innermost 1 kpc regions are excluded, for which $\alpha^*_{CC} = 0.65 \pm 0.26$.

We conclude there is a significant trend detected of declining ϵ_{orb} with increasing β, i.e., reduced SFE per orbit as the rate of shear decreases. Furthermore, the functional form of this trend agrees well with the prediction of the shear-driven GMC collision theory of J. C. Tan (2000). The result is insensitive to whether or not the innermost annuli are excluded or whether galaxy-normalized quantities are used. Thus, our results are

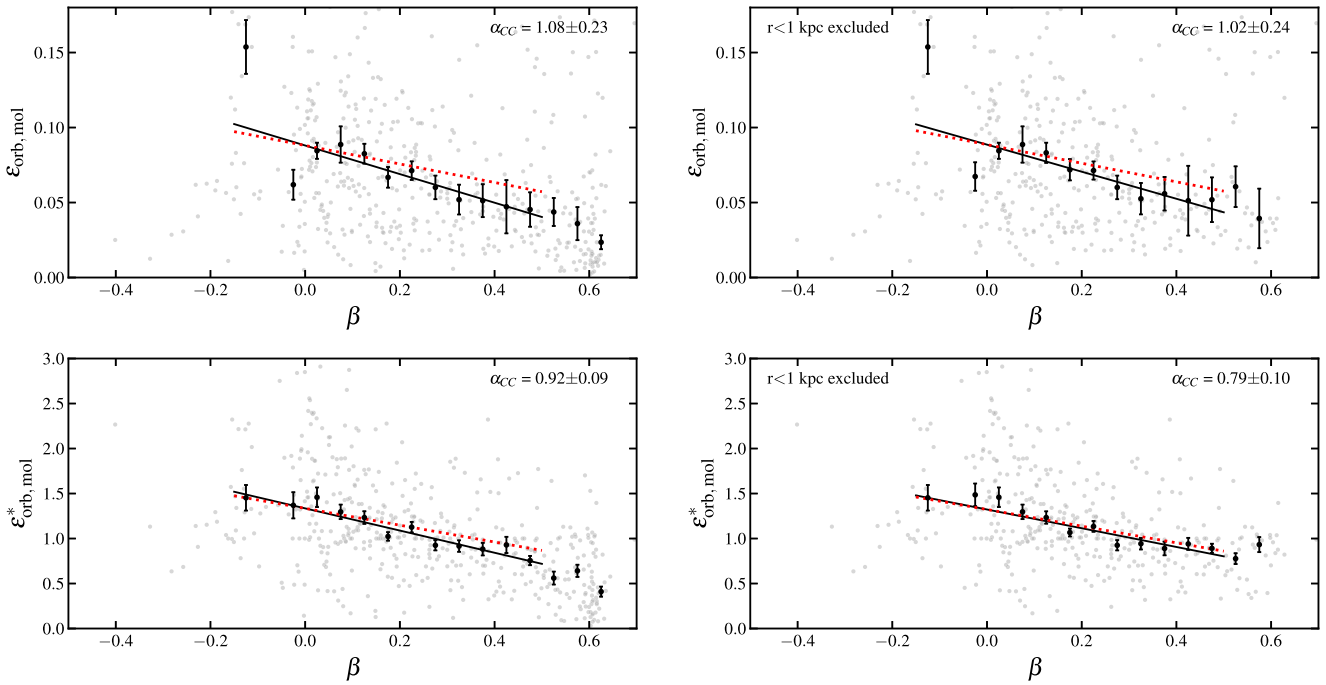

Figure 3. (a) Top left: SFE from molecular gas per orbit, $\epsilon_{\rm orb,mol}$, vs. rotation curve gradient, β, for 489 annuli located in 49 PHANGS-ALMA galaxies (gray points). Median values of $\epsilon_{\rm orb,mol}$ in bins of $\Delta\beta = 0.05$ that have $\geqslant$10 data points are shown by black points, with uncertainties shown by the error bars. The best-fitting function of the form $\epsilon_{\rm orb,mol} = \epsilon_{\rm orb,mol,0}(1 - \alpha_{\rm CC,mol}\beta)$ to median values with $\beta \leqslant 0.5$ is shown by the solid black line, with $\alpha_{\rm CC,mol}$ reported in the upper right. The red dotted line shows the equivalent fit when $\alpha_{\rm CC,mol} = 0.7$. (b) Top right: as (a), but now excluding annuli within $r = 1$ kpc. (c) Bottom left: as (a), but now showing the "galaxy-normalized efficiency," $\epsilon^*_{\rm orb,mol}$. (d) Bottom right: as (c), but now excluding annuli within $r = 1$ kpc.

evidence in favor of shear-driven GMC collisions being the primary mechanism regulating star formation in galactic disks.

Our results agree with those of C. Suwannajak et al. (2014), who found $\alpha_{\rm CC} = 1.13 \pm 0.49$ for their full data set based on older observations for 16 galaxies (which overlaps partially, 7/16, with our sample), or $\alpha_{\rm CC} = 1.10 \pm 0.44$ when innermost annuli were excluded. For galaxy-normalized data, C. Suwannajak et al. (2014) found $\alpha^*_{\rm CC} = 1.39 \pm 0.32$ and $\alpha^*_{\rm CC} = 1.35 \pm 0.31$ for the full and inner-kiloparsec-excluded data sets, respectively. Their larger values of $\alpha_{\rm CC}$ and $\alpha^*_{\rm CC}$ could be related to systematic differences in analysis methods. In particular, we use a more realistic, metallicity-dependent conversion factor of CO line luminosity to molecular gas mass, which tends to reduce our gas masses in inner, high-β regions, thus causing $\epsilon_{\rm orb}$ to increase in this regime and thus reducing our value of $\alpha_{\rm CC}$ compared to that of C. Suwannajak et al. (2014).

In Figure 3 we repeat the above analysis, but now considering $\epsilon_{\rm orb,mol}$ across 489 independent annuli in 49 PHANGS-ALMA galaxies. We find $\epsilon_{\rm orb,mol,0} = 0.088 \pm 0.005$ and $\alpha_{\rm CC,mol} = 1.08 \pm 0.23$. Excluding the innermost 1 kpc has only a minor effect, with $\alpha_{\rm CC,mol} = 1.02 \pm 0.24$. For the galaxy-normalized data, we find $\alpha^*_{\rm CC,mol} = 0.92 \pm 0.09$. Excluding the innermost 1 kpc yields $\alpha^*_{\rm CC,mol} = 0.79 \pm 0.10$. These slightly larger values of $\alpha_{\rm CC}$ in the molecular case are likely caused by the atomic gas making up a larger fraction of the total in the outer regions that tend to have smaller values of β. Thus, SFE per orbit with respect to molecular gas is larger in these low-β regions, resulting in a steeper gradient in the $\epsilon_{\rm orb,mol}$ versus β plane.

In summary, the results of Figure 3 indicate a clear decrease in SFE per orbit with increasing β when only considering the molecular gas, similar to our conclusion for the total gas.

3.2. Impact of a Bar on Star Formation

To test the effect of a stellar bar on $\epsilon_{\rm orb}$, we divide the measurements into two subsamples, i.e., annuli that do and do not overlap with the footprint of a stellar bar (as characterized by M. Querejeta et al. 2021; also see J. Sun et al. 2022). We note that this comparison only measures the potential impact of a bar on SFE assessed in global annular averages. Overall, for regions with both atomic and molecular data, the barred/nonbarred samples consist of 143/178 annuli, respectively. For the SFE from molecular gas analysis, barred/nonbarred samples consist of 194/295 annuli, respectively.

Figure 4 shows these data, distinguishing between barred/nonbarred data. We evaluate the median values of $\epsilon_{\rm orb}$ of these subsamples. The barred sample has $\overline{\epsilon_{\rm orb}} = 0.0324 \pm 0.0017$ and the nonbarred has $\overline{\epsilon_{\rm orb}} = 0.0375 \pm 0.0015$. Thus, the barred sample shows a reduced SFE relative to the nonbarred by a factor of 0.86. The median values of β of the barred and nonbarred subsamples are 0.364 ± 0.022 and 0.117 ± 0.012, respectively. For these values of β and for $\alpha_{\rm CC} = 0.76$, Equation (6) predicts that the barred sample would have lower SFE per orbit than the nonbarred sample by a factor of 0.79. Thus, the differences we see between the barred and nonbarred samples are attributable to the difference in their β ranges, i.e., the lower shear of barred regions explains their reduced SFE per orbit.

We repeat the above analysis, but now considering $\epsilon_{\rm orb,mol}$. Evaluating median values for $\epsilon_{\rm orb,mol}$ of these subsamples we find $\overline{\epsilon_{\rm orb,mol}} = 0.0425 \pm 0.0025$ for the barred sample and $\overline{\epsilon_{\rm orb,mol}} = 0.0780 \pm 0.0039$ for the nonbarred. Again, the presence of a bar is associated with reduced SFE per orbit, now by a factor of 0.54. The median values of β of these barred/nonbarred subsamples are $0.370 \pm 0.021/0.165 \pm 0.013$. For these values of β and for $\alpha_{\rm CC,mol} = 1.08$,

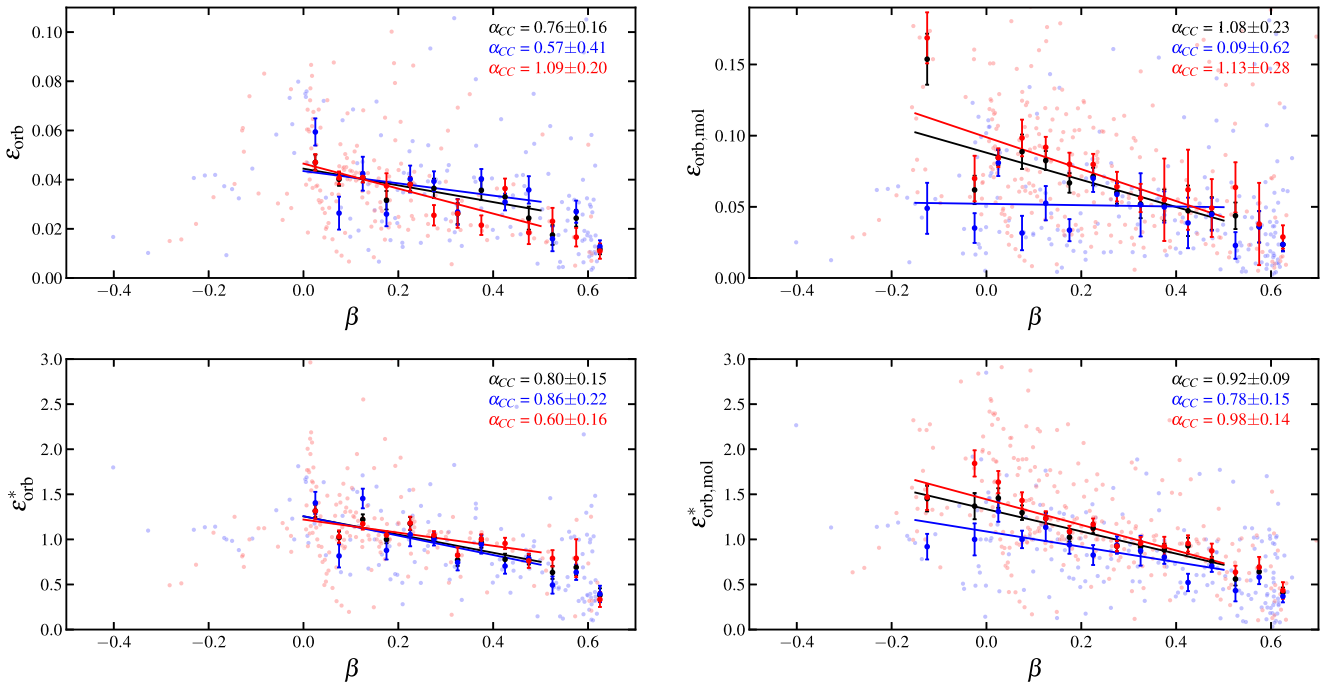

Figure 4. (a) Top left: similar to Figure 2(a), total SFE per orbit, ϵ_{orb}, vs. rotation curve gradient, β, for 32 PHANGS-ALMA galaxies with molecular and atomic gas data. Barred/nonbarred annuli are shown in blue/red, respectively. Median values of ϵ_{orb} of the combined sample in bins of $\Delta\beta = 0.05$ with $\geqslant$10 data points are shown by black points. In this range of β, we also show medians of barred/nonbarred annuli with dark blue/red points, respectively. Best-fitting functions to the medians of form $\epsilon_{orb} = \epsilon_{orb,0}(1 - \alpha_{CC}\beta)$ are shown by the black, blue, and red lines for total, barred, and nonbarred samples, respectively. (b) Top right: as (b), but now for SFE from molecular gas per orbit, $\epsilon_{orb,mol}$, vs. β, for 49 PHANGS-ALMA galaxies. (c) Bottom left: as (a), but now showing "galaxy-normalized efficiency", ϵ^*_{orb}. (d) Bottom right: as (b), but now showing $\epsilon^*_{orb,mol}$.

Equation (6) predicts that the barred sample would have lower SFE per orbit than the nonbarred sample by a factor of 0.73. Thus, most of the observed reduction is attributable to the lower shear of the barred regions, but with a tentative hint of an additional suppression of SFE in those regions.

To further investigate the dependence of SFE with shear in the barred/nonbarred samples and compare with fitted parameters of Section 3.1, we again turn to binned statistics and focus on data with $\beta < 0.5$. In Figure 4 we show fits for the barred/nonbarred subsamples across the same set of β bins used for fitting the global trend. This conserves the information content of the original sample. The barred sample has $\epsilon_{orb,0} = 0.043 \pm 0.007$ and $\alpha_{CC} = 0.57 \pm 0.41$, while the nonbarred sample has $\epsilon_{orb,0} = 0.047 \pm 0.003$ and $\alpha_{CC} = 1.09 \pm 0.20$. For the galaxy-normalized data, the barred sample has $\alpha^*_{CC} = 0.86 \pm 0.22$, while the nonbarred sample has $\alpha^*_{CC} = 0.60 \pm 0.16$. We see that barred and nonbarred samples have best-fit parameters that are consistent with each other within the uncertainties.

When considering $\epsilon_{orb,mol}$, the barred sample has $\epsilon_{orb,mol,0} = 0.052 \pm 0.008$ and $\alpha_{CC,mol} = 0.09 \pm 0.62$, while the nonbarred sample has $\epsilon_{orb,mol,0} = 0.099 \pm 0.007$ and $\alpha_{CC,mol} = 1.13 \pm 0.28$. For the galaxy-normalized data, the barred sample has $\alpha^*_{CC,mol} = 0.78 \pm 0.15$, while the nonbarred sample has $\alpha^*_{CC,mol} = 0.98 \pm 0.14$. From this, we see the dependence of $\epsilon_{orb,mol}$ on shear is greater in the nonbarred sample: in particular, in the high shear regime with $\beta \simeq 0$ the SFE per orbit is larger in nonbarred environments. However, we caution that the significance of this effect is modest. There are also known systematic biases (e.g., bar dynamics affecting rotation curve measurements, biases in SFR, and gas mass estimates near galaxy centers; see P. Lang et al. 2020; J. Sun et al. 2023) that impact the barred and nonbarred samples differently. These systematic effects could potentially explain at least part of the apparent differences in the observed trends.

4. Summary and Discussion

We have investigated SFE per orbit, ϵ_{orb}, with reference to total gas content, and how it depends on the local rate of shear, as parameterized by $\beta \equiv d \ln v_{circ}/d \ln r$ in 32 galaxies from the PHANGS-ALMA survey. We have found clear evidence for a decline in ϵ_{orb} as the rate of shear decreases, i.e., as β increases from near zero of the flat rotation curve regime toward $\beta \sim 1$ of the solid body rotation regime. Such a trend is the opposite of that expected if the growth of gravitational instabilities is the rate-limiting step for galactic disk star formation (e.g., B. G. Elmegreen 1991).

Motivated by a prediction of the shear-driven GMC collision theory of J. C. Tan (2000), we fit a function $\epsilon_{orb} = \epsilon_{orb,0}(1 - \alpha_{CC}\beta)$ to the data where $\beta \leqslant 0.5$. The shear-driven GMC collision model predicts $\alpha_{CC} = 0.7$; we find $\alpha_{CC} = 0.76 \pm 0.16$ or $\alpha_{CC} = 0.73 \pm 0.21$ when inner kiloparsec regions are excluded. For a fit to efficiencies normalized by the median value in each galaxy, we find $\alpha^*_{CC} = 0.80 \pm 0.15$ and $\alpha^*_{CC} = 0.65 \pm 0.26$ when inner kiloparsec regions are excluded. For SFE per orbit with respect to molecular gas, similar but slightly larger values of α_{CC} are derived. Thus, our primary conclusion is that the observational data are consistent with the theoretical prediction of the shear-driven GMC collision model, implying that this process may play an important, perhaps dominant, role in controlling galactic disk SFRs.

As reviewed by J. C. Tan et al. (2013), there are important implications for the evolution of GMCs and the interstellar medium (ISM) of galaxies if shear-driven GMC collisions occur

at a high enough rate to trigger most star formation in galactic disks. In the shear-driven GMC collision model, the formation of molecular gas, i.e., GMCs, from atomic gas is not the rate-limiting step for star formation. Indeed, a significant fraction ($\gtrsim 1/3$) of the disk ISM, which is self-regulated by star formation activity to have Toomre $Q \sim 1$, is assumed to be in GMCs that are relatively stable with respect to collapse due to the presence of magnetic fields and turbulence. Frequent collisions between GMCs create local regions that lose magnetic support, i.e., becoming magnetically supercritical, and collapse with relatively high efficiency to form star clusters and associations. This process then sets the clustering properties of star formation, especially making the distribution of young stars more clustered than that of molecular gas. The stochastic nature of GMC collisions leads to a broad dispersion in GMC SFEs based on instantaneous snapshots of current young star populations and associated local molecular gas, which helps explain observed distributions of efficiencies in GMCs (e.g., J. C. Tan 2000; E. J. Lee et al. 2016). The kinematics of these young stars are expected to be quite disturbed, which aligns with observational results from Gaia proper motion studies of Galactic young stars (N. J. Wright et al. 2023).

In addition, frequent shear-driven collisions between GMCs are efficient at extracting galactic orbital kinetic energy and converting it into turbulent kinetic energy in the clouds, giving additional support to much of their structures. Thus GMCs, even though containing significant amounts of locally self-gravitating gas, are typically not globally relaxed and virialized, i.e., on the largest scales a single "GMC" is often composed of two or more self-gravitating clouds interacting from a recent collision that overall can appear to be unbound. Another consequence of frequent collisions of GMCs is a broad distribution of angular momentum directions, including significant fractions with retrograde rotation with respect to their galaxy (E. J. Tasker & J. C. Tan 2009; Q. Li et al. 2018), which appears relevant to observations of Milky Way (N. Imara & L. Blitz 2011) and nearby galaxy (E. Rosolowsky et al. 2003; N. Imara et al. 2011) GMC populations. Finally, since collisions are driven by galactic shear, this causes large-scale dense filamentary substructures of the GMCs to have preferential alignment with the galactic plane (M. J. Butler et al. 2015), which is observed in samples of large ($\gtrsim$10 pc) Galactic filaments (e.g., C. Zucker et al. 2018; Y. Ge et al. 2023).

Previous studies have disfavored GMC collisions as an important mechanism because of supposedly long timescales for GMCs to collide compared to estimated GMC lifetimes (e.g., C. F. McKee & E. C. Ostriker 2007; J. Sun et al. 2022). However, since the scale height of molecular gas is similar to GMC sizes, their collision times need to be estimated in a 2D geometry in a shearing disk (C. F. Gammie et al. 1991; J. C. Tan 2000; E. J. Tasker & J. C. Tan 2009; Q. Li et al. 2018) rather than a 3D geometry (e.g., C. F. McKee & E. C. Ostriker 2007). Collision times in regions where a significant fraction ($\gtrsim 1/3$) of total ISM mass is in GMCs are estimated to be ~10%–20% of a local orbital time (J. C. Tan 2000; E. J. Tasker & J. C. Tan 2009; Q. Li et al. 2018), which is ~10–30 Myr in the regions considered in our study (J. Sun et al. 2022). We note that the observational estimates of GMC collision times by J. Sun et al. (2022), although based on a 2D disk geometry, are still likely overestimated, since the number of clouds per unit area is limited by the data resolution and effects of gravitational focusing were not included (i.e., collision cross section should be ~1–2 tidal radii, which can be larger than cloud geometric sizes; see C. F. Gammie et al. 1991; J. C. Tan 2000). Finally, the relatively short estimates of GMC lifetimes (~5–30 Myr) based on the spatial decorrelation between CO and Hα emission (a.k.a. the "tuning fork" method; e.g., A. Schruba et al. 2010; J. M. D. Kruijssen & S. N. Longmore 2014; M. Chevance et al. 2020; J. Kim et al. 2022) have recently been called into question by J. Koda & J. C. Tan (2023), especially in molecular-rich regions, as the observed CO–Hα decorrelation can also be reproduced if GMCs and their young stars have modest relative drift speeds of $\sim 10\,\mathrm{km\,s^{-1}}$ (however, see a counterclaim by J. M. D. Kruijssen et al. 2024). Such drift speeds can potentially be induced by the GMC collision process itself. Thus, given the uncertainties, we consider that current estimates of GMC collision times and lifetimes are comparable and a scenario in which GMC evolution is significantly affected by frequent collisions is plausible.

Future studies are needed to further investigate and test predictions of the shear-driven GMC theory. For example, a larger set of high-resolution observations that focuses on regions of low and high shear will help to test the theory more stringently. Regions of higher shear, i.e., where the rotation curve is declining with radius, should yield a greater dynamic range in predicted SFRs and SFEs. However, if the relative speed of collisions increases in such regions, then the impact of this increased collision speed on the SFE from a given collision may need to be accounted for.

On the other hand, in low-shear regions of near solid body rotation, i.e., with $\beta \sim 1$, shear-driven GMC collisions will not occur frequently enough to influence star formation and other processes must instead regulate the process. Thus, in these regions, relevant to galactic centers, late-type spiral galaxies, and dwarf galaxies, one expects potentially significant systematic differences in star formation properties, including efficiency per orbit, efficiency per local free-fall time, and the initial cluster mass function (ICMF). The results presented here are the most extensive to date focusing on the impact on $\epsilon_{\rm orb}$ in these low-shear regions, with the overall value dropping by a factor of at least ~0.6 for regions with $\beta > 0.5$ compared to the flat rotation curve ($\beta = 0$) regime. In terms of the impact on the ICMF, J. D. Dowell et al. (2008) investigated whether it differs in large disk galaxies compared to dwarf galaxies, finding ICMFs were indistinguishable for masses $>10^{4.4}\,M_\odot$. However, to our knowledge, an explicit investigation of the ICMF as a function of β remains to be carried out.

Finally, there are other environments in which shear-driven GMC collisions are not expected to be important and where star formation properties may also differ from typical disk systems. These include "overlap" regions of colliding galaxies, e.g., in the Antennae galaxies (e.g., B. C. Whitmore et al. 2014; N. Brunetti et al. 2024), although GMC collisions may still be occurring driven by flows associated with the galaxy collision. Tidal tails of interacting or stripped galaxies (e.g., B. M. Poggianti et al. 2019) are other environments where shear-driven collisions are not expected to operate and star formation would be regulated by alternative processes. Systematic studies of samples of such sources and comparison to galactic disks are promising avenues to better understand the processes regulating star formation across diverse galactic environments.

Acknowledgments

We thank constructive inputs from the anonymous referee and the ApJ statistics editor. X.F.B. acknowledges support from a Virginia Initiative on Cosmic Origins (VICO) summer undergraduate fellowship and support from the Chalmers Initiative on Cosmic Origins (CICO). J.S. acknowledges support by the National Aeronautics and Space Administration (NASA) through the NASA Hubble Fellowship grant HST-HF2-51544 awarded by the Space Telescope Science Institute (STScI), operated by the Association of Universities for Research in Astronomy, Inc., under contract NAS 5-26555. J.C.T. acknowledges support from NSF grant AST-2009674 and ERC Advanced Grant MSTAR.

This paper makes use of the following ALMA data, which have been processed as part of the PHANGS-ALMA CO(2–1) survey: ADS/JAO.ALMA#2012.1.00650.S, ADS/JAO.ALMA#2015.1.00925.S, ADS/JAO.ALMA#2015.1.00956.S, ADS/JAO.ALMA#2017.1.00392.S, ADS/JAO.ALMA#2017.1.00886.L, and ADS/JAO.ALMA#2018.1.01651.S. ALMA is a partnership of ESO (representing its member states), NSF (USA), and NINS (Japan), together with NRC (Canada), NSC and ASIAA (Taiwan), and KASI (Republic of Korea), in cooperation with the Republic of Chile. The Joint ALMA Observatory is operated by ESO, AUI/NRAO, and NAOJ. The National Radio Astronomy Observatory (NRAO) is a facility of NSF operated under cooperative agreement by Associated Universities, Inc. (AUI).

This work is based in part on observations made with NSF's Karl G. Jansky Very Large Array (VLA; project code: 14A-468, 14B-396, 16A-275, 17A-073, 18B-184). VLA is also operated by NRAO.

This work makes use of data products from the Wide-field Infrared Survey Explorer (WISE), a joint project of the University of California, Los Angeles, and the Jet Propulsion Laboratory/California Institute of Technology, funded by NASA.

This work is based in part on data gathered with the CIS 2.5 m Irénée du Pont Telescope and the ESO/MPG 2.2 m Telescope at Las Campanas Observatory, Chile.

Facilities: ALMA, VLA, WISE, Du Pont, Max Planck:2.2m.

Software: `NumPy` (C. R. Harris et al. 2020), `Matplotlib` (J. D. Hunter 2007), `astropy` (Astropy Collaboration et al. 2013, 2018, 2022).

ORCID iDs

Jiayi Sun (孙嘉懿) https://orcid.org/0000-0003-0378-4667
Jonathan C. Tan https://orcid.org/0000-0002-3389-9142

References

Astropy Collaboration, Price-Whelan, A. M., Lim, P. L., et al. 2022, ApJ, 935, 167
Astropy Collaboration, Price-Whelan, A. M., Sipőcz, B. M., et al. 2018, AJ, 156, 123
Astropy Collaboration, Robitaille, T. P., Tollerud, E. J., et al. 2013, A&A, 558, A33
Belfiore, F., Leroy, A. K., Sun, J., et al. 2023, A&A, 670, A67
Bigiel, F., Leroy, A., Walter, F., et al. 2008, AJ, 136, 2846
Binney, J., & Tremaine, S. 1987, Galactic Dynamics (Princeton, NJ: Princeton Univ. Press)
Brunetti, N., Wilson, C. D., He, H., et al. 2024, MNRAS, 530, 597
Butler, M. J., Tan, J. C., & Van Loo, S. 2015, ApJ, 805, 1
Chevance, M., Kruijssen, J. M. D., Hygate, A. P. S., et al. 2020, MNRAS, 493, 2872
Chung, A., van Gorkom, J. H., Kenney, J. D. P., Crowl, H., & Vollmer, B. 2009, AJ, 138, 1741
Dowell, J. D., Buckalew, B. A., & Tan, J. C. 2008, AJ, 135, 823
Elmegreen, B. G. 1991, ApJ, 378, 139
Elmegreen, B. G. 1997, RMxAA, 6, 165
Gammie, C. F., Ostriker, J. P., & Jog, C. J. 1991, ApJ, 378, 565
Ge, Y., Wang, K., Duarte-Cabral, A., et al. 2023, A&A, 675, A119
Harris, C. R., Millman, K. J., van der Walt, S. J., et al. 2020, Natur, 585, 357
Hunter, J. D. 2007, CSE, 9, 90
Imara, N., Bigiel, F., & Blitz, L. 2011, ApJ, 732, 79
Imara, N., & Blitz, L. 2011, ApJ, 732, 78
Kennicutt, R. C., & Evans, N. J. 2012, ARA&A, 50, 531
Kennicutt, R. C. J. 1998, ApJ, 498, 541
Kim, J., Chevance, M., Kruijssen, J. M. D., et al. 2022, MNRAS, 516, 3006
Koda, J., & Tan, J. C. 2023, ApJ, 959, 1
Kruijssen, J. M. D., Chevance, M., Longmore, S. N., et al. 2024, arXiv:2404.14495
Kruijssen, J. M. D., & Longmore, S. N. 2014, MNRAS, 439, 3239
Krumholz, M. R., McKee, C. F., & Tumlinson, J. 2009, ApJ, 699, 850
Lang, P., Meidt, S. E., Rosolowsky, E., et al. 2020, ApJ, 897, 122
Lee, E. J., Miville-Deschênes, M.-A., & Murray, N. W. 2016, ApJ, 833, 229
Leroy, A. K., Bigiel, F., de Blok, W. J. G., et al. 2012, AJ, 144, 3
Leroy, A. K., Schinnerer, E., Hughes, A., et al. 2021, ApJS, 257, 43
Leroy, A. K., Walter, F., Brinks, E., et al. 2008, AJ, 136, 2782
Li, Q., Tan, J. C., Christie, D., Bisbas, T. G., & Wu, B. 2018, PASJ, 70, S56
McKee, C. F., & Ostriker, E. C. 2007, ARA&A, 45, 565
Poggianti, B. M., Gullieuszik, M., Tonnesen, S., et al. 2019, MNRAS, 482, 4466
Querejeta, M., Schinnerer, E., Meidt, S., et al. 2021, A&A, 656, A133
Rosolowsky, E., Engargiola, G., Plambeck, R., & Blitz, L. 2003, ApJ, 599, 258
Schinnerer, E., & Leroy, A. K. 2024, arXiv:2403.19843
Schruba, A., Leroy, A. K., Walter, F., et al. 2011, AJ, 142, 37
Schruba, A., Leroy, A. K., Walter, F., Sandstrom, K., & Rosolowsky, E. 2010, ApJ, 722, 1699
Silk, J. 1997, ApJ, 481, 703
Sun, J., Leroy, A. K., Ostriker, E. C., et al. 2020a, ApJ, 892, 148
Sun, J., Leroy, A. K., Ostriker, E. C., et al. 2023, ApJL, 945, L19
Sun, J., Leroy, A. K., Rosolowsky, E., et al. 2022, AJ, 164, 43
Sun, J., Leroy, A. K., Schinnerer, E., et al. 2020b, ApJL, 901, L8
Suwannajak, C., Tan, J. C., & Leroy, A. K. 2014, ApJ, 787, 68
Tan, J. C. 2000, ApJ, 536, 173
Tan, J. C. 2010, ApJL, 710, L88
Tan, J. C., Shaske, S. N., & Van Loo, S. 2013, in IAU Symp., Vol. 292, Molecular Gas, Dust, and Star Formation in Galaxies, ed. T. Wong & J. Ott (Cambridge: Cambridge Univ. Press), 19
Tasker, E. J., & Tan, J. C. 2009, ApJ, 700, 358
Walter, F., Brinks, E., de Blok, W. J. G., et al. 2008, AJ, 136, 2563
Whitmore, B. C., Brogan, C., Chandar, R., et al. 2014, ApJ, 795, 156
Wright, N. J., Kounkel, M., Zari, E., Goodwin, S., & Jeffries, R. D. 2023, in ASP Conf. Ser. 534, Protostars and Planets VII, ed. S. Inutsuka et al. (San Francisco, CA: ASP), 129
Wyse, R. F. G., & Silk, J. 1989, ApJ, 339, 700
Zucker, C., Battersby, C., & Goodman, A. 2018, ApJ, 864, 153